A Double-Receiver Compact SCC-WPT System With CV/CC Output for Mobile Devices Charging/Supply

Zhe Liu, Hongsheng Hu, *Member, IEEE*, Yu-Gang Su, *Member, IEEE*, Yue Sun, *Member, IEEE*, Fengwei Chen, and Pengqi Deng

***Abstract*—The single capacitance coupled wireless power transfer (SCC-WPT) technology facilitates improving the spatial freedom of the system to offer charging/supply services in 2-D planar. This article proposes a double-receiver SCC-WPT system with three-plate compact coupler to achieve free-position charging and superior system performance. The system consists of two independent receivers: one receiver adopts the *LCLC*-S topology to achieve constant-voltage (CV) output, while the other adopts the *LCLC*-M topology to achieve constant-current (CC) output and did not affect each other. By circuit analysis, a simplified equivalent circuit of the three-plate coupler is established and, on this basis, the CV and CC characteristics are theoretically analyzed. The effectiveness of the proposed system is verified by building a prototype system, where the coupler and parameters are designed and optimized. The experimental results show that the two receivers can realize CV output and CC output, respectively. The output characteristic of each receiver is almost unchanged when another receiver is removed or moved in. The receiver can obtain stable output power at any position within the transmitting plate.**

***Index Terms*—Compact coupler, constant output characteristic, double-receiver, receiver independent, single capacitance coupled wireless power transfer (SCC-WPT).**

I. Introduction

CAPACITIVE power transfer (CPT) technology is a kind of wireless power transfer (WPT) technology with metal plates as a coupler and a high-frequency electric field as the power carrier. Due to the coupler having the advantages of being lightweight, thin, low-cost, and low eddy-current losses in the surrounding metallic objects, CPT technology has attracted much attention [1], [2], [3].

CPT technology has been well studied and developed in several research fields, including compensation networks, coupling structure, parameter design and optimization, modeling, and dynamic analysis [4], [5], [6], [7], [8]. Most previous studies focus on conventional CPT systems, which need two pairs of metal plates to form the circuit loop. However, the flexibility of the coupling structure could be restricted due to the cross-capacitance between each pair of metal plates, especially for applied in 2-D plane dynamic mobile devices [9], [10], [11].

In recent years, especially for mobile device applications, the system is required to have the capability of spatial degree of freedom, powering multiple independent devices, different constant output characteristics, etc. [12], [13], [14] Some studies have achieved free-positioning feature by designing coupled structures or using switching controls, but they struggle to maintain stable performance under rotational offset [15], [16]. Supplied power to multiple devices in mobile devices has always been urgent. Compared with the IPT technology, CPT systems use a metal plate as the coupling structure, which is less expensive and avoids the problem of heat generation [17], [18], [19]. However, due to the influence of cross-coupling capacitance between the misaligned transmitting plate and receiving plate, the single transmitter and multiple receivers (STMRs) system with conventional CPT topology can only work in well-aligned conditions or in cases where the receiver only moves freely in one dimension [20], [21]. In contrast, the single capacitance coupled wireless power transfer (SCC-WPT) technology could overcome this problem and has a higher degree of mobility, which is more suitable for the STMR system.

The SCC-WPT technology forms a complete electrical loop with the ground by using the stray capacitance of the components on the secondary side and the self-capacitance of the metal plate [22], [23]. This technology has many advantages, such as reducing the number of coupling plates, improving space utilization, and avoiding cross-coupling of the metal plates. Thus, the technology facilitates improving the spatial freedom of the system to offer power supply services in two-dimensional (2-D). In [24], two metallic balls through a virtual self-capacitance route are used to enhance the system, and the transfer distance of the system is greater than the size of the coupler. In [25], with the help of the stray capacitance between the chassis of the electric vehicles and the ground as the current return route, the system will still work effectively. Meanwhile, reducing the number of plates also could be achieved when applied in some special applications. For example, in railway EVs and power transmission line monitoring, the primary side of the system can connect or equivalently short-connect the secondary side

Manuscript received 14 December 2022; revised 25 February 2023; accepted 3 April 2023. Date of publication 11 April 2023; date of current version 19 May 2023. This work was supported by the research funds for the National Natural Science Foundation of China under Grant 51977015 and Grant 62073246. Recommended for publication by Associate Editor M. Vitelli. *(Corresponding author: Hongsheng Hu.)*

Zhe Liu, Hongsheng Hu, Fengwei Chen, and Pengqi Deng are with the School of Automation, Chongqing University, Chongqing 400044, China (e-mail: 809632730@qq.com; huhongsheng@cqu.edu.cn; fengwei.chen@cqu.edu.cn; 357619947@qq.com).

Yu-Gang Su and Yue Sun are with the School of Automation, Chongqing University, Chongqing 400044, China, and also with the China National Center for International Research on Wireless Power Transfer Technology, Chongqing 400044, China (e-mail: su7558@qq.com; syue@cqu.edu.cn).

Color versions of one or more figures in this article are available at https://doi.org/10.1109/TPEL.2023.3266270.

Digital Object Identifier 10.1109/TPEL.2023.3266270

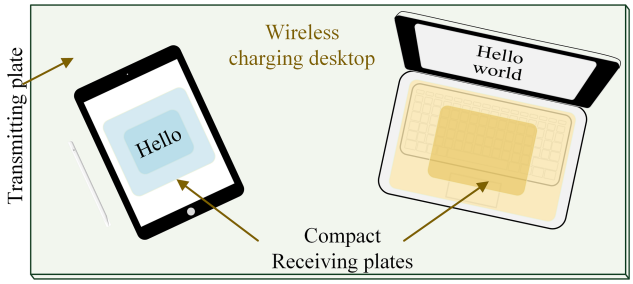

Fig. 1. Wireless charging desktop with the compact coupler of the SCC-WPT system.

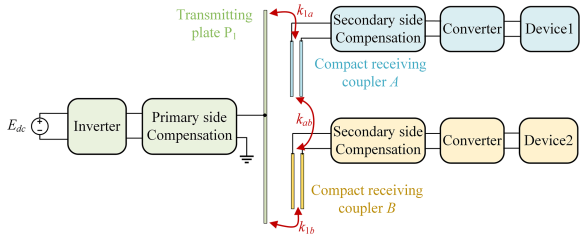

Fig. 2. Structure of double-receiver compact SCC-WPT.

[26], [27]. However, the previous study about the SCC-WPT technology focuses on the single transmits and single receiver system, and the STMR system with SCC-WPT technology has not been studied.

To fill the blank of the research in this area, this article proposes an SCC-WPT system with double receivers, where the power transfer to each receiver is independent of the other receiver. Besides, the two receivers can realize constant-voltage (CV) output and constant-current (CC) output, respectively. Fig. 1 shows a wireless charging desktop with the compact coupler of the SCC-WPT system. The transmitting plate only needs one metal plate by adopting SCC-WPT technology, and the receiver could be moved freely within the range of the transmitting plate. The secondary side of the mobile device usually needs integration, the stray capacitance of the secondary side being small and thus resulting in deterioration of transmission performance of the SCC-WPT system [23]. Therefore, a three-plate compact coupler is proposed to increase coupling capacitance and improve the system's performance. The double-receiver SCC-WPT has five metal plates in total, and the three-plate compact coupler is aimed at one receiver. Then the capacitive model of the system is analyzed based on the multiport network method. The simplified equivalent model of the double-receiver SCC-WPT system is established. According to the simplified equivalent model, the compensation network with different constant output characteristics is proposed, and the resonance relationship of the system is analyzed. In addition, the compact coupler is analyzed by using the finite element simulation software. At last, the experiments verify the correctness of the theory.

This article proposed a double-receiver SCC-WPT system with load-independent characteristics and CV/CC output for the mobile device. The rest of this article is organized as follows. Section II analyzes the double-receiver full capacitance model and derives the equivalent circuit model. Based on the equivalent circuit, the different constant output characteristics with the double-receiver SCC-WPT system are introduced in Section III. Section IV studies the double-receiver's compact coupler and provides the parameter design method of the system. The experimental results are provided in Section V. Finally, Section VI concludes the article.

II. Capacitive Model and its Circuit Model

A. Double-Receiver Coupler

Fig. 2 shows the topology of the proposed double-receiver compact SCC-WPT. The transmitting side and secondary side are coupling with each other, and the $k_{1\,a}$, $k_{1\,b}$, and k_{ab} represent the coupling coefficients of the transmitting plate with receiving coupler A, the transmitting plate with receiving coupler B, and receiving coupler A with B, respectively. The transmitting plate only needs a metal plate P_1 on the primary side. The receiving plate adopts a compact coupler, in which the metal plates are stacked to save space, thus improving the power density. When the plate is charged and the distance is far less than the size of the plates, the charge distribution becomes that of an isolated plate. The electrostatic potential energy of the two equally charged plates approaches that of a single plate containing double the charge. Therefore, the capacitance C_{plate} between each coupling plate and the ground approaches half of their self-capacitances when the distance between the metal plates and the ground is far greater than the size of the metal plates [28], [29]

$$C_{\text{plate}} = \frac{1}{2}C_{\text{plate\_self}} = \frac{2\varepsilon_0 p}{3\pi}\left(1+\sqrt{1+\frac{12\pi s}{p^2}}\right) \tag{1}$$

where $\varepsilon_0 = 8.85 \times 10$–$12$ F/m is the permittivity of free space, p and s represent the perimeter of the metal plate and the area of the metal plate, respectively. In addition, every two plates will form a capacitance. Thus, the coupler of double receivers has a total number of 15 equivalent capacitances, including coupling capacitance, cross capacitance, and self-capacitance, as shown in Fig. 3. The receiving coupler of receiver A consist of plates P_2 and P_3, and the receiving coupler of receiver B consist of plates P_4 and P_5.

B. Three-Port Circuit Model of Double-Receiver Coupler

According to Fig. 3, the three-port circuit model of the double-receiver coupler can be established, as shown in Fig. 4(a), in which $\mathbf{U}_1$ is the voltage on the primary side, $\mathbf{U}_a$ and $\mathbf{U}_b$ are the voltage on the receiving coupler A and B, respectively. The $\mathbf{I}_1$, $\mathbf{I}_a$, and $\mathbf{I}_b$ present the current on the primary side of the coupler, the current on the receiving coupler A and the current on the receiving coupler B, respectively. The model can be considered as a three-port network.

In Fig. 4(b), the Nodal Analysis method is adopted, with the ground side being defined as the reference node. The relation

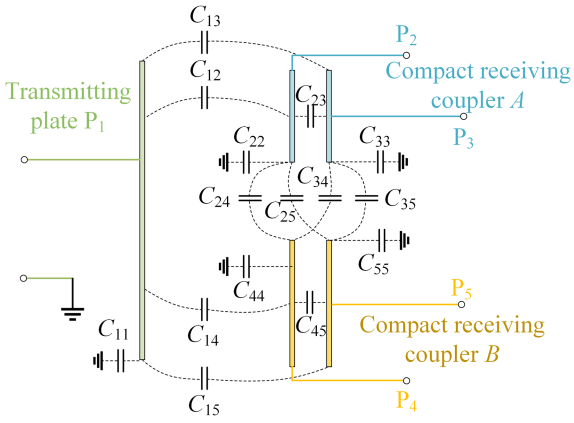

Fig. 3. Full-capacitance of double-receiver coupler.

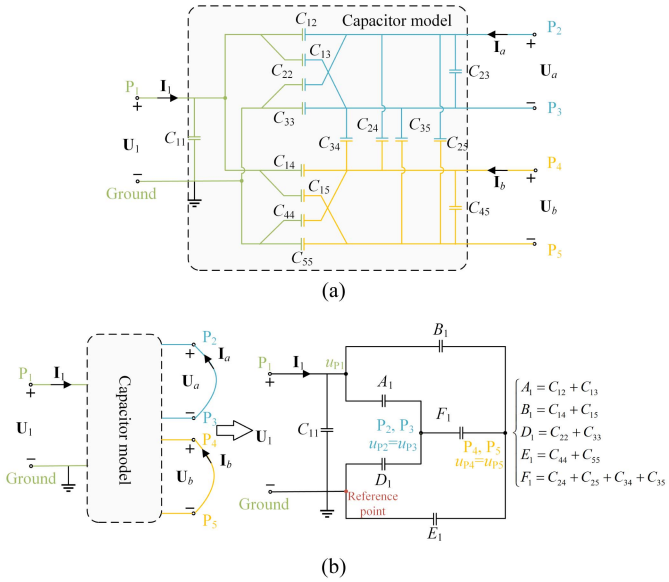

Fig. 4. Circuit model (a) three-port circuit model of coupler. (b) Nodal Analysis for model when $\mathbf{U}_a = \mathbf{U}_b = 0$.

between the input current and the node voltage can be expressed as

$$\begin{bmatrix} C_{11}+A_1+B_1 & -A_1 & -B_1 \\ -A_1 & A_1+D_1+F_1 & -F_1 \\ -B_1 & -F_1 & B_1+E_1+F_1 \end{bmatrix} \begin{bmatrix} u_{p1} \\ u_{P2} \\ u_{p4} \end{bmatrix} = \begin{bmatrix} I_1/j\omega \\ 0 \\ 0 \end{bmatrix} \tag{2}$$

and

$$\begin{cases} A_1 = C_{12}+C_{13} \\ B_1 = C_{14}+C_{15} \\ D_1 = C_{22}+C_{33} \\ E_1 = C_{44}+C_{55} \\ F_1 = C_{24}+C_{25}+C_{34}+C_{35} \end{cases} \tag{3}$$

where C_{11}, C_{22}, C_{33}, C_{44}, and C_{55} are the self-capacitance of each plate; C_{12}, C_{13}, and C_{23} are the coupling capacitance of receiver A; C_{14}, C_{15}, and C_{45} are the coupling capacitance of receiver B; C_{24}, C_{25}, C_{34} and C_{35} are the cross capacitance between receiver A and receiver B.

According to (2) and (3), the node voltage u_{p2} and u_{p4} are expressed as

$$\begin{aligned} u_{p2} = u_{p3} &= \frac{A_1B_1+A_1E_1+A_1F_1+B_1F_1}{(A_1+B_1+D_1+E_1)F_1+(A_1+D_1)(B_1+E_1)}u_{p1} \\ u_{p4} = u_{p5} &= \frac{A_1B_1+A_1F_1+B_1D_1+B_1F_1}{(A_1+B_1+D_1+E_1)F_1+(A_1+D_1)(B_1+E_1)}u_{p1}. \end{aligned} \tag{4}$$

In addition, the currents $\mathbf{I}_a$ and $\mathbf{I}_b$ are expressed below according to Fig. 4

$$\begin{aligned} \mathbf{I}_a &= j\omega(C_{13}u_{p1} - (C_{13}+C_{33}+C_{34}+C_{35})u_{p3} \\ &\quad + (C_{34}+C_{35})u_{p5}) \\ \mathbf{I}_b &= j\omega(C_{15}u_{p1} + (C_{25}+C_{35})u_{p3} \\ &\quad - (C_{15}+C_{25}+C_{35}+C_{55})u_{p5}). \end{aligned} \tag{5}$$

The admittance Y represent the ratio of current and voltage, according to (5), the admittance parameters Y_{11}, Y_{21}, and Y_{31} are defined as follows:

$$\begin{cases} Y_{11} = \left.\dfrac{\mathbf{I}_1}{\mathbf{U}_1}\right|_{\mathbf{U}_a=\mathbf{U}_b=0} = j\omega C_1 \\ Y_{21} = \left.\dfrac{\mathbf{I}_a}{\mathbf{U}_1}\right|_{\mathbf{U}_a=\mathbf{U}_b=0} = -j\omega C_{Ma1} \\ Y_{31} = \left.\dfrac{\mathbf{I}_b}{\mathbf{U}_1}\right|_{\mathbf{U}_a=\mathbf{U}_b=0} = -j\omega C_{Mb1} \end{cases} \tag{6}$$

where C_1 is the equivalent capacitance of the primary side, C_{Ma1}, and C_{Mb1} are the mutual capacitances between primary side and receiving coupler A or B, and the C_1, C_{Ma1}, and C_{Mb1} are expressed as (7) shown at the bottom of the next page.

Therefore, other Y-parameters could be calculated through the same light of analysis. The admittance parameters Y_{12}, Y_{22}, and Y_{32} can be obtained when the voltage $\mathbf{U}_1$ and $\mathbf{U}_b$ are set to zero. Meanwhile, the parameters Y_{13}, Y_{23}, and Y_{33} are acquired with $\mathbf{U}_1$ and $\mathbf{U}_a$ are zero. These parameters and the equations are given in Table V, as shown in Appendix. It should be emphasized that some parameters are equal according to the reciprocity theory, as shown

$$\begin{cases} C_{M1a} = C_{Ma1} \\ C_{M1b} = C_{Mb1} \\ C_{Mab} = C_{Mba} \\ C_{X1} = C_{Xa} = C_{Xb} \end{cases}. \tag{8}$$

According to the above analysis, the relationship between current and voltage of the three-port could be obtained as

$$\begin{cases} \mathbf{I}_1 = Y_{11}\mathbf{U}_1 + Y_{12}\mathbf{U}_a + Y_{13}\mathbf{U}_b \\ \mathbf{I}_a = Y_{21}\mathbf{U}_1 + Y_{22}\mathbf{U}_a + Y_{23}\mathbf{U}_b \\ \mathbf{I}_b = Y_{31}\mathbf{U}_1 + Y_{32}\mathbf{U}_a + Y_{33}\mathbf{U}_b \end{cases}. \tag{9}$$

Thus, a 3×3 matrix about the terminal voltage and current is expressed as

$$\mathbf{I} = \begin{bmatrix} \mathbf{I}_1 \\ \mathbf{I}_a \\ \mathbf{I}_b \end{bmatrix} = \begin{bmatrix} Y_{11} & Y_{12} & Y_{13} \\ Y_{21} & Y_{22} & Y_{23} \\ Y_{31} & Y_{32} & Y_{33} \end{bmatrix} \begin{bmatrix} \mathbf{U}_1 \\ \mathbf{U}_a \\ \mathbf{U}_b \end{bmatrix} = \mathbf{YU}. \tag{10}$$

The coupling coefficient of coupler can be defined as

$$\begin{cases} k_{1a} = C_{M1a}/\sqrt{C_1 C_a} \\ k_{1b} = C_{M1b}/\sqrt{C_1 C_b} \\ k_{ab} = C_{Mab}/\sqrt{C_a C_b} \end{cases} \tag{11}$$

where C_a and C_b are the equivalent capacitance of the receiving coupler *A* and receiving coupler *B*.

According to (10), the matrix *G*-parameters of the three-port network are calculated to facilitate the analysis. The relation between the terminal current and voltage is expressed as

$$\begin{bmatrix} \mathbf{I}_1 \\ \mathbf{U}_a \\ \mathbf{U}_b \end{bmatrix} = \begin{bmatrix} G_{11} & G_{12} & G_{13} \\ G_{21} & G_{22} & G_{23} \\ G_{31} & G_{32} & G_{33} \end{bmatrix} \begin{bmatrix} \mathbf{U}_1 \\ \mathbf{I}_a \\ \mathbf{I}_b \end{bmatrix} = \mathbf{G} \begin{bmatrix} \mathbf{U}_1 \\ \mathbf{I}_a \\ \mathbf{I}_b \end{bmatrix} \tag{12}$$

where

$$\begin{cases} G_{11} = j\omega C_1 C_a C_b k_m / C_x \\ G_{22} = -C_b / j\omega C_x \\ G_{33} = -C_a / j\omega C_x \\ G_{12} = -G_{21} = (C_{M1a} C_b + C_{M1b} C_{Mab}) / C_x \\ G_{13} = -G_{31} = (C_{M1b} C_a + C_{M1a} C_{Mab}) / C_x \\ G_{23} = G_{32} = -C_{Mab} / j\omega C_x \\ k_m = k_{1a}^2 + k_{1b}^2 + k_{ab}^2 + 2k_{1a}k_{1b}k_{ab} - 1 \\ C_x = C_{Mab}^2 - C_a C_b \end{cases}. \tag{13}$$

C. Equivalent Circuit Model When Applied in Mobile Device

The mobile device often needs to move in or be removed frequently in practical applications. In this regard, the system needs to have a load-independent characteristic to ensure safe and reliable device operation, i.e., a device should keep constant power when the other device is moved in or removed. According (12), each output depends on the output with the other two ports. The primary side and secondary sides are coupled with each other. In practice, the charging air gap of mobile devices is relatively small, such as mobile phones, laptops, and some desktop applications.

The capacitance of the square and rectangular capacitors can be calculated according to [30] when considering the edge effects

$$\begin{cases} C_S = [1 + 2.343 \cdot (d/l)^{0.891}] \cdot (\varepsilon \cdot l^2 / d) \\ C_r = [1 + 2.343 \cdot (d \cdot w/L)^{0.891}] \cdot (\varepsilon \cdot L \cdot w/d) \end{cases} \tag{14}$$

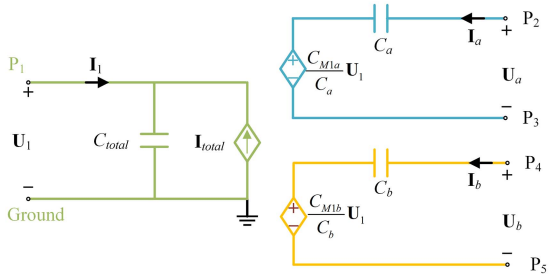

Fig. 5. Simplified equivalent model of the double-receiver coupler with controlled source.

where *d* is the distance between two plates. The *l* is the length of the square plate, *w* and *L* are the width and length of the rectangular capacitor, respectively.

From (14), the value of capacitance is determined by the area of two metal plates. The receiving plate of receivers *A* and *B* are basically on the same plane, and the thickness is just 1mm. A small positive area leads to a very small capacitance value. In this situation, the mutual capacitance of the coupler will be far greater than the cross capacitance between the two receiving couplers. It should be noted that the cross capacitance refers the capacitance between one plate of receiving coupler *A* with one plate of receiving coupler *B*. Therefore, the cross capacitance of C_{24}, C_{25}, C_{34}, C_{35} and C_{Mab} could be ignored when the transmitting distance is small, i.e., Thus, the parameters of the coupler can be simplified as

$$\begin{cases} C_1 = C_{11} + \frac{B_1 E_1}{B_1 + E_1} + \frac{A_1 D_1}{A_1 + D_1} \\ C_a = C_{23} + \frac{B_2 E_2}{B_2 + E_2} \\ C_b = C_{45} + \frac{A_3 D_3}{A_3 + D_3} \\ C_{M1a} = C_{Ma1} = \frac{C_{12} C_{33} - C_{13} C_{22}}{B_2 + E_2} \\ C_{M1b} = C_{Mb1} = \frac{C_{14} C_{55} - C_{15} C_{44}}{A_3 + D_3} \end{cases}. \tag{15}$$

At this time, the receivers are independent of each other, and the output characteristics of the devices are only determined by the primary side output voltage $\mathbf{U}_1$. When the device is moved in or removed, as long as the voltage $\mathbf{U}_1$ remains constant, the output characteristics of the other device can remain unchanged. Therefore, the equivalent circuit of the double-receiver coupler can be simplified, as shown in Fig. 5. The terminal voltages and currents of the three ports are represented as $\mathbf{U}_1$, $\mathbf{I}_1$, $\mathbf{U}_a$, $\mathbf{I}_a$, $\mathbf{U}_b$, and $\mathbf{I}_b$. In Fig. 5, the parameters of C_{total} and $\mathbf{I}_{\text{total}}$ are defined as

$$\begin{cases} C_{\text{total}} = C_{ex1} + C_1(1 - k_{1a}^2 - k_{1b}^2) \\ \mathbf{I}_{\text{total}} = \frac{C_{M1a}}{C_a}\mathbf{I}_a + \frac{C_{M1b}}{C_b}\mathbf{I}_b \end{cases}. \tag{16}$$

$$\begin{cases} C_{X1} = (A_1 + B_1 + D_1 + E_1)F_1 + (A_1 + D_1)(B_1 + E_1) \\ C_1 = C_{11} + \frac{A_1((B_1+F_1)(D_1+E_1)+D_1E_1)+B_1(D_1F_1+D_1E_1+E_1F_1)}{C_{X1}} \\ C_{Ma1} = \frac{(C_{12}C_{33}-C_{13}C_{22})(B_1+E_1+F_1)+(C_{24}+C_{25})(B_1C_{33}-E_1C_{13})+(C_{34}+C_{35})(E_1C_{12}-B_1C_{22})}{C_{X1}} \\ C_{Mb1} = \frac{C_{55}(A_1B_1+A_1F_1+B_1D_1+B_1F_1)-C_{15}(A_1E_1+D_1E_1+D_1F_1+E_1F_1)-(C_{25}+C_{35})(A_1E_1-B_1D_1)}{C_{X1}} \end{cases}. \tag{7}$$

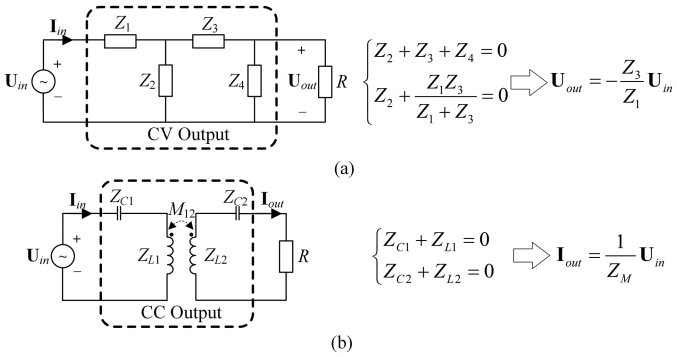

Fig. 6. CV and CC circuit. (a) CV output network and (b) CC output network with voltage source.

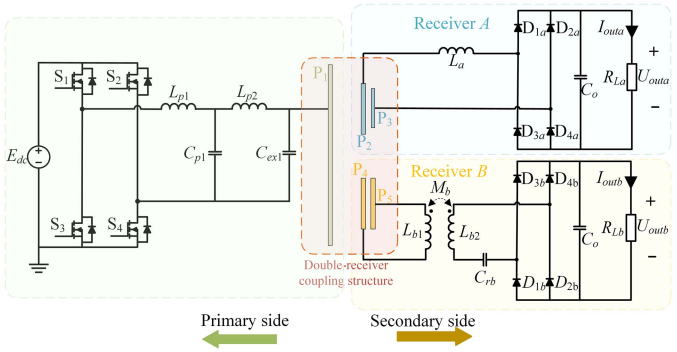

Fig. 7. Topology of double-receiver compact SCC-WPT system.

III. Model of Double-Receiver SCC-WPT System

A. Equivalent Circuit of the Double-Receiver System

Some devices often require constant output characteristics in practical applications. The system achieving CV output without affecting the zero-phase angle needs to adopt the fourth-order compensation network when the voltage-type inverter is used [19]. Meanwhile, the series-series mutual inductance circuit could achieve a CC output, and the output current depends on the mutual inductance M_{12} [31]. The resonance relationship is shown in Fig. 6(a) and (b). In Fig. 6(a), Z_1, Z_2, Z_3, and Z_4 are the impedance element, and they can only be composed of two capacitors and two inductors when the constant voltage output is required. In Fig.6(b), Z_{C1} and Z_{C2} are capacitance impedance; Z_{L1} and Z_{L2} are inductance impedance; Z_M is mutual impedance, and $Z_M = j\omega M_{12}$.

A double-receiver SCC-WPT system with constant output is proposed based on the above analysis, where CV output and CC output can be achieved simultaneously in the different receivers. Fig. 7 shows the proposed double-receiver SCC-WPT system with the inverter and rectifier.

In Fig. 7, the primary side consists of a dc power source $E_{\rm dc}$, a full-bridge inverter composed of four power MOSFETs S_1-S_4, the *LCLC* resonant network, and transmitting plate P_1, The *LCLC* resonant network includes inductor L_{p1} and L_{p2}, capacitor C_{p1}, and C_{ex1}. The system connects to the earth's ground through the primary side. Receiver *A* consists of receiving coupler *A*, inductor L_a, and a full-bridge rectifier with diodes D_1, D_2, D_3, and D_4 followed by a resistor R_L. Receiver *B* consists of receiving coupler *B*, inductor L_{b1}, inductor L_{b2}, capacitor C_{rb} and full-bridge rectifier with diodes D_1, D_2, D_3, and D_4 followed by a resistor R_L; M_b is the mutual inductance of L_{b1} and L_{b2}. The parameters $U_{\text{out}\,a}$, $I_{\text{out}\,a}$, $U_{\text{out}\,b}$, and $I_{\text{out}\,b}$ are represented as dc output voltage of receiver *A*, dc output current of receiver *A*, dc output voltage of receiver *B*, and dc output current of receiver *B*, respectively.

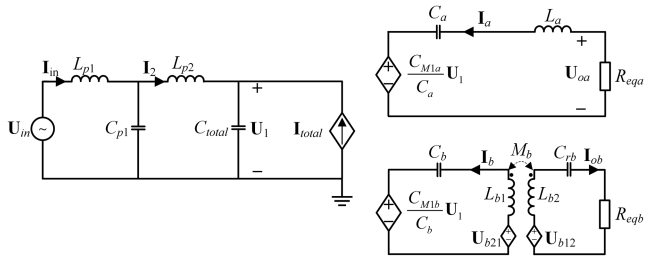

Fig. 8. Equivalent circuit of the double-receiver SCC-WPT system.

The *LCLC* compensation network could achieve CV output according to the analysis in Fig. 6. In the compensation of the secondary side, the *S*-type compensation network is adopted to achieve CV mode, and the *M*-type compensation network is adopted to achieve CC output. The double-receiver coupler consists of the transmitting plate P_1 and receiving plates P_2, P_3, P_4, and P_5. The equivalent circuit for Fig. 7 is obtained and shown in Fig. 8. In Fig. 8, the voltage $\mathbf{U}_{\rm in}$ is the equivalent ac input voltage. The current $\mathbf{I}_{\rm in}$, $\mathbf{I}_2$, $\mathbf{I}_a$, $\mathbf{I}_{b,}$ and $\mathbf{I}_{ob}$ are represented as input current, current of L_{p2}, output current of receiver *A*, current of L_{b1}, and output current of receiver *B*, respectively. $\mathbf{U}_{b21}$ and $\mathbf{U}_{b12}$ are the controlled source of voltage. $R_{\rm eq}$ is the effective ac resistance presented by the rectifier and the load resistance. Ideally, the rectifier input current is sinusoidal and the diode forward voltage drop is ignored. According to the principle of power equivalence, the following equation can be obtained [32]

$$R_{\rm eq} = \frac{8}{\pi^2} R_{\rm L}. \tag{17}$$

In addition, the voltage of $\mathbf{U}_{b12}$ and $\mathbf{U}_{b21}$ are as defined as

$$\begin{cases} \mathbf{U}_{b12} = -j\omega M_b \mathbf{I}_b \\ \mathbf{U}_{b21} = -j\omega M_b \mathbf{I}_{ob} \end{cases}. \tag{18}$$

B. CV Mode

According to the above analysis, when the receiver is required to work in the CV mode, the parameters of the system need to satisfy the following equation:

$$\begin{cases} j\omega L_{p2} + 1/j\omega C_{p1} + 1/j\omega C_{\rm total} = 0 \\ 1/j\omega C_{p1} + \frac{j\omega L_{p1} \cdot j\omega L_{p2}}{j\omega L_{p1} + j\omega L_{p2}} = 0 \\ j\omega L_a + 1/j\omega C_a = 0 \end{cases}. \tag{19}$$

According to (19), the voltage $\mathbf{U}_1$ is calculated as below, which is independent of the load resistance

$$\mathbf{U}_1 = -\frac{L_{p2}}{L_{p1}}\mathbf{U}_{\text{in}}. \tag{20}$$

The output voltage of receiver *A* is derived as

$$\mathbf{U}_{oa} = -\frac{L_{p2}}{L_{p1}} \cdot \frac{C_{M1a}}{C_a}\mathbf{U}_{\text{in}}. \tag{21}$$

Thus, the gain of output voltage on receiver *A* is provided as

$$G_{va} = \left|\frac{\mathbf{U}_{oa}}{\mathbf{U}_{\text{in}}}\right| = \frac{L_{p2}}{L_{p1}} \cdot \frac{C_{M1a}}{C_a}. \tag{22}$$

From (22), the output voltage is independent of the load resistance R_{La}, i.e., the system could work in CV mode. Combining with (19), the output power of the receiver *A* can be derived as

$$P_{\text{out}a} = \frac{\pi^2 L_{p2}^2 C_{M1a}^2}{8L_{p1}^2 C_a^2 R_{La}} U_{\text{in}}^2. \tag{23}$$

C. CC Mode

Similarly, the parameters of the system need to satisfy the following equation when the CC output characteristic is achieved

$$\begin{cases} j\omega L_{b1} + 1/j\omega C_b = 0 \\ j\omega L_{b2} + 1/j\omega C_{rb} = 0 \end{cases}. \tag{24}$$

Then the voltage relationship can be derived as

$$\begin{cases} \frac{C_{M1b}}{C_b}\mathbf{U}_1 = -\left(\frac{1}{j\omega C_b} + j\omega L_{b1}\right)\mathbf{I}_b - j\omega M_b \mathbf{I}_{ob} \\ 0 = \left(\frac{1}{j\omega C_{rb}} + R_{eqb} + j\omega L_b\right)\mathbf{I}_{ob} + j\omega M_b \mathbf{I}_b \\ M_b = k_b\sqrt{L_{b1}L_{b2}} \end{cases} \tag{25}$$

where k_b represents the coefficient of mutual induction of L_{b1} and L_{b2}.

Thus, the current of the secondary side with receiver *B* is expressed as

$$\begin{cases} \mathbf{I}_{ob} = \frac{L_{p2}}{L_{p1}} \cdot \frac{C_{M1b}\mathbf{U}_{in}}{j\omega M_b C_b} \\ \mathbf{I}_b = \frac{L_{p2}}{L_{p1}} \cdot \frac{R_{\text{eqb}} C_{M1b}\mathbf{U}_{\text{in}}}{\omega^2 M_b^2 C_b} \end{cases}. \tag{26}$$

From (26), the gain of the output current on the receiver *B* is obtained as

$$G_{ib} = \left|\frac{\mathbf{I}_{ob}}{\mathbf{U}_{\text{in}}}\right| = \frac{L_{p2}}{L_{p1}} \cdot \frac{C_{M1b}}{\omega M_b C_b}. \tag{27}$$

By combining (17) and (26), the output power of the receiver *B* can be derived as

$$P_{\text{out}b} = \frac{8L_{p2}^2 C_{M1b}^2}{\pi^2\omega^2 M_b^2 C_b^2 L_{p1}^2} R_{Lb} U_{\text{in}}^2. \tag{28}$$

The output power of the system depends on the number of the receiver. The input power is equal to the sum of the output power of each receiver when the parasitic resistance is ignored, and the output power of the double-receiver system is derived as

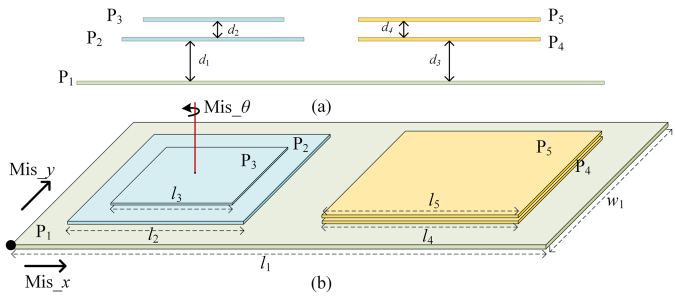

Fig. 9. Coupler of the double-receiver compact system (a) lateral view and (b) 3-D view.

TABLE I
COUPLER PARAMETERS

Symbol	Parameter	Value
l_1	Length of Transmitting plate P_1	1000 mm
w_1	width of Transmitting plate P_1	500 mm
l_2	Side length of plate P_2	0–400 mm
l_3	Side length of plate P_3	0–400 mm
l_4	Side length of plate P_4	0–400 mm
l_5	Side length of plate P_5	0–400 mm
d_1, d_3	Transmission distance	5 mm
d_2	Distance between P_2 and P_3	0–5 mm
d_4	Distance between P_4 and P_5	0–5 mm

as

$$P_{\text{out}} = P_{\text{out}a} + P_{\text{out}b} = \frac{L_{p2}^2 U_{\text{in}}^2}{L_{p1}^2}\left(\frac{\pi^2 C_{M1a}^2}{8R_{La}C_a^2} + \frac{8C_{M1b}^2 R_{Lb}}{\pi^2\omega^2 M_b^2 C_b^2}\right). \tag{29}$$

Therefore, the currents of transmitting side in the system can be expressed as

$$\begin{cases} \mathbf{I}_{\text{in}} = \frac{L_{p2}^2}{L_{p1}^2}\left(\frac{\pi^2 C_{M1a}^2}{8R_{La}C_a^2} + \frac{8C_{M1b}^2 R_{Lb}}{\pi^2\omega^2 M_b^2 C_b^2}\right)\mathbf{U}_{\text{in}} \\ \mathbf{I}_2 = \left(1 - \omega^2 L_{p1} C_{p1}\right)\mathbf{I}_{\text{in}} \end{cases}. \tag{30}$$

IV. DESIGN OF DOUBLE-RECEIVER SCC-WPT SYSTEM

A. Design of the Double-Receiver Coupler

According to (23) and (28), when the system works in the CV mode, the output power $P_{\text{out}a}$ depends on the ratio of capacitors $C_{M1\text{a}}$ and C_a when the input voltage and inductor are determined. The output power $P_{\text{out}b}$ is related to the capacitor C_{M1b} when the system works in the CC mode. Therefore, it is necessary to design the coupler to improve the system output power.

Fig. 9 shows the coupler of the double-receiver compact system. In order to illustrate the analysis, select a 1000 mm×500 mm aluminum plate as a primary side plate P_1. Select the square aluminum plates as receiving plates, and Table I gives the size of the coupler. The Ansoft Maxwell is used to simulate the coupler, and the thickness of each aluminum plate is 1mm. Therefore, the mutual capacitance between each plate could be obtained. According to (1) and (15), the mutual capacitances C_{M1a} and C_{M1b} could be calculated, and then the capacitances C_1, C_a, and C_b can also be obtained. The two receiving coupler show the same characteristic and results in

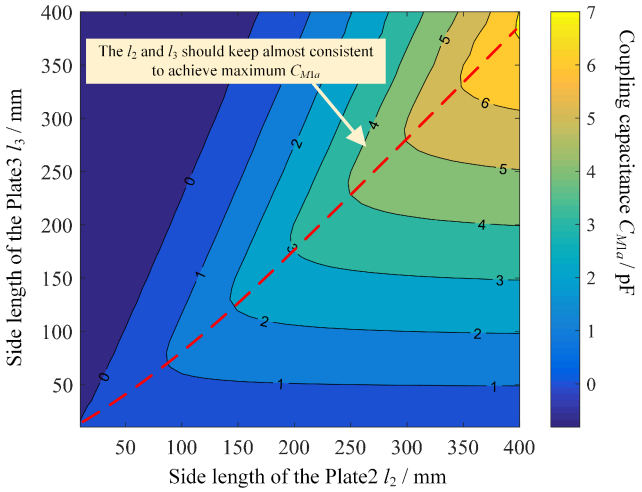

Fig. 10. Simulated parameter $C_{M1\,a}$ with the l_2 and l_3, when the distance d_1 and d_2 with 5 mm distance.

the simulation. Therefore, the simulation results of only one receiver are given.

The transmission distance d_1 is often determined by the requirements of the application. In this simulation, the distance is set to 5 mm considering the thickness of the protective case and the fuselage shell in practical application. When the side length of the receiving plate varies from 0 to 400 mm with the distance d_2 being 5 mm, the simulated results are shown in Fig. 10. The mutual capacitance $C_{M1\,a}$ can achieve maximum value when the side length of P_2 and P_3 is equal. By contrast, increasing the size of P_2 is easier to increasing the mutual capacitance $C_{M1\,a}$. When l_2 and l_3 are set to 400 mm, the mutual capacitance $C_{M1\,a}$ is about 7.03 pF.

Meanwhile, the results of capacitance C_a and the ratio $C_{M1\,a}/C_a$ are also calculated, as shown in Fig. 11(a) and (b). From Fig. 11(a), the capacitance C_a increases as the l_2 and l_3 increase. When the side length of plate l_2 and l_3 is selected to 400 mm, the C_a is about 318 pF. From Fig. 11(b), the ratio $C_{M1\,a}/C_a$ increased as the l_2 increased, and the l_3 increase will lead to the decrease of $C_{M1\,a}/C_a$. When the l_2 is 400 mm, and the l_3 is 300 mm, the ratio is about 0.03. According to (23), in the CV mode, the output power depends on the ratio $C_{M1\,a}/C_a$. The higher the ratio is, the greater the output power $P_{\text{out}\,a}$ can be. Therefore, l_2 should be selected as large as possible, and l_3 should be minimized when the system works in CV mode. Note that C_a decreases with the decrease of l_3, and this will result in an increase in the resonant inductor L_b.

The design of the coupler needs to analyze the distance d_2. Fig. 12 shows the simulated parameter $C_{M1\,a}$, capacitance C_a, and ratio $C_{M1\,a}/C_a$ with the distance d_2. The mutual capacitance $C_{M1\,a}$ remained almost unchanged when the distance d_2 varied. In addition, the capacitance C_a decreases with the increase of distance d_2. By contrast, the ratio $C_{M1\,a}/C_a$ increases with increasing distance d_2, and the smaller l_3, the faster the ratio increases.

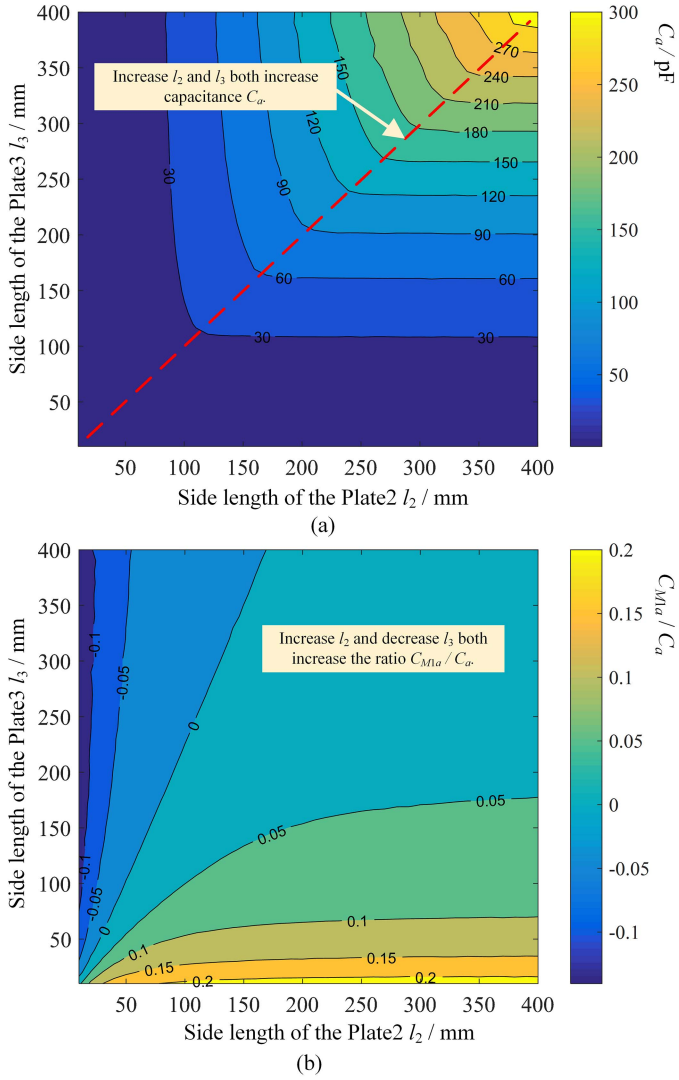

Fig. 11. Simulated parameters of coupler with the l_2 and l_3, when the distance d_1 and d_2 with 5mm distance. (a) Capacitance C_a (b) ratio of $C_{M1\,a}/C_a$.

In conclusion, when the system works in the CV mode, the side length l_2 need to be selected as large as possible, and l_3 should be reduced. But, side length l_3 too small will cause C_a decrease, resulting in an increase in the volume and size of the resonant inductor L_a. To further increase the ratio $C_{M1\,a}/C_a$, the distance d_2 could be increased appropriately.

When the system works in the CC mode, according to (28), the output power not only depends on the ratio $C_{M1\,b}/C_b$, but also could be adjusted by the mutual inductance M_{12}. Therefore, the value of capacitance C_b is plays a dominant role for output power regulation. To increase capacitance C_b, the side lengths l_4, and l_5 need to keep consistent and be selected as large as possible. Meanwhile, reducing the distance d_1 could obtain a large capacitor C_b, and further reduce the volume and size of the inductor L_{b1}.

According to the experimental condition in our laboratory, the size of the transmitting plate P_1 is $1000\times500\times1$ mm. Based

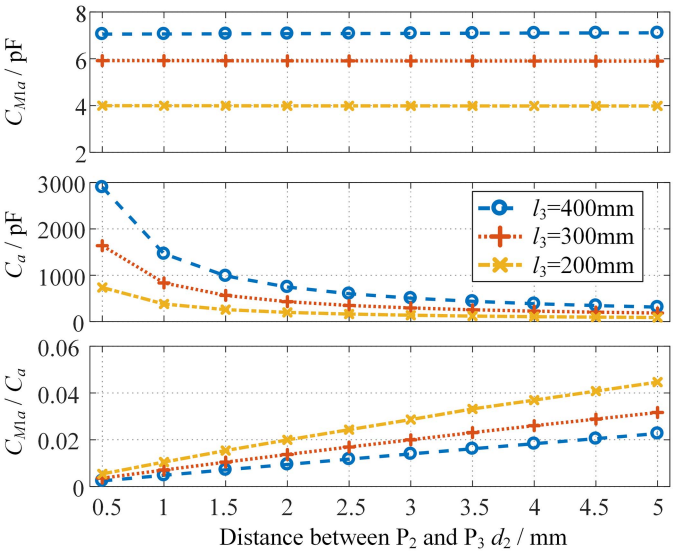

Fig. 12. Simulated parameter $C_{M1\,a}$, C_a and ratio $C_{M1\,a}/C_a$ with the distance d_2, when the distance d_1 with 5 mm and l_2 with 400 mm.

TABLE II
PARAMETERS OF CAPACITOR

Symbol	Value	Symbol	Value
C_{11}	15.54 pF	C_1	45.91 pF
C_{22}	8.51 pF	C_{44}	8.51 pF
C_{33}	6.38 pF	C_{55}	8.51 pF
C_{12}	310.67 pF	C_{14}	295.03 pF
C_{13}	4.3 pF	C_{15}	19.24 pF
C_{23}	175.92 pF	C_{45}	482.6 pF
C_a	186.26 pF	C_b	508 pF
C_{M1a}	5.9 pF	C_{M1b}	7.08 pF
k_{1a}	0.063	k_{1b}	0.046

on the above analysis, the sizes of plates P_2 and P_4 are set to 400 mm×400 mm×1 mm, and the sizes of plates P_3 and P_5 are chosen to be 300 mm×300 mm×1 mm and 400 mm×400 mm×1 mm, respectively. The transfer distance d_1 and d_3 is set to 5 mm, the distance d_2 is 5mm, and the distance d_4 is 3mm. The simulated capacitances and calculated results are given in Table II.

B. Maxwell Simulation of Free-Positioning Feature

For the free-positioning feature of the proposed system, three misalignment axes are defined in Fig. 9, i.e., Mis_x, Mis_y, and Mis_θ. The original point is set at the bottom left corner. The receiving coupler A and receiving coupler B moved in the range of transmitting plate P_1 are simulated by using Ansoft Maxwell, as shown in Fig. 13. The mutual capacitance $C_{M1\,a}$ and coupling coefficient $k_{1\,a}$ are basically unchanged when the receiving coupler A at different positions. Only slight changes occur when moving to the corner of the P_1, and the rate of change is lower than 1%. The mutual capacitance $C_{M1\,b}$ and coupling coefficient $k_{1\,b}$ can also maintain constant, the rate of change with $C_{M1\,b}$ is lower than 2%, and the $k_{1\,b}$ is almost unchanged.

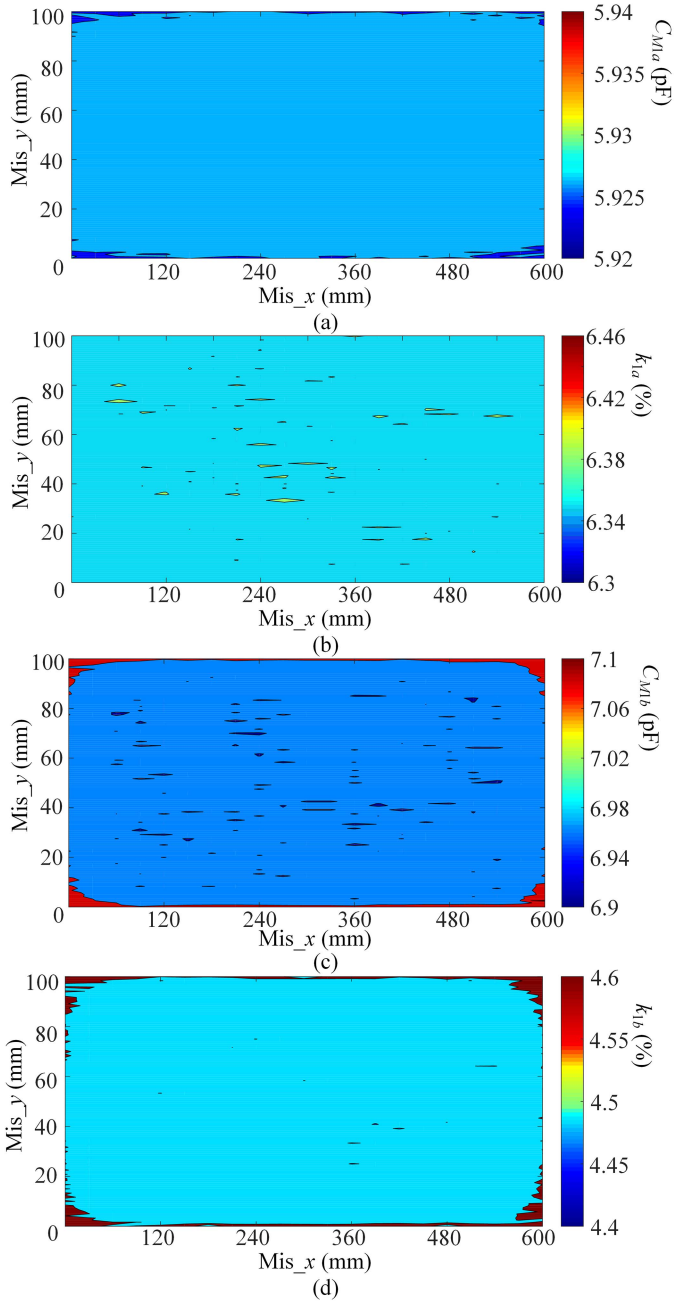

Fig. 13. Simulated results of (a) mutual capacitance $C_{M1\,a}$, (b) coupling coefficient $k_{1\,b}$, (c) mutual capacitance $C_{M1\,b}$, and (d) coupling coefficient $k_{1\,b}$ within range of transmitting plate.

Fig. 14 shows the simulated results of $C_{M1\,a}$, $C_{M1\,b}$, $k_{1\,a}$, and $k_{1\,b}$ in the rotational offset cases when the Mis_x = 300 mm and Mis_y = 50 mm. When the rotation angle θ exceeds 20 degrees, the receiving plate has exceeded the width of the transmitting plate P_1; even so, the parameters $C_{M1\,a}$, $C_{M1\,b}$, $k_{1\,a}$, and $k_{1\,b}$ can still keep stable.

C. Design Method of the System

The parameter design method of the system can be obtained according to the above results. Fig. 15 shows the associated

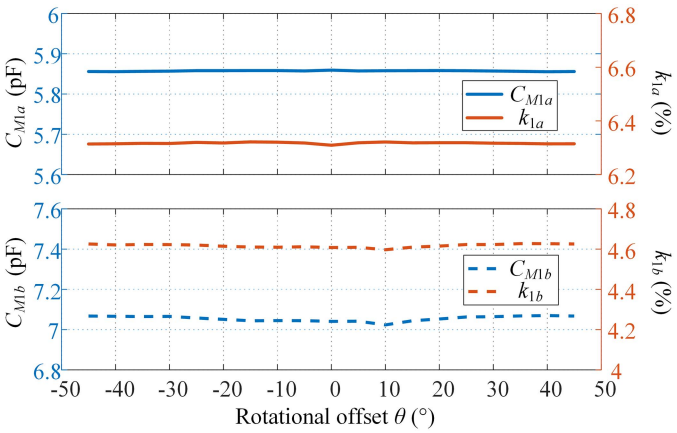

Fig. 14. Simulated results of $C_{M1\,a}$, $C_{M1\,b}$, $k_{1\,a}$, and $k_{1\,b}$ in the rotational offset cases when the Mis_x = 300 mm and Mis_y = 50 mm.

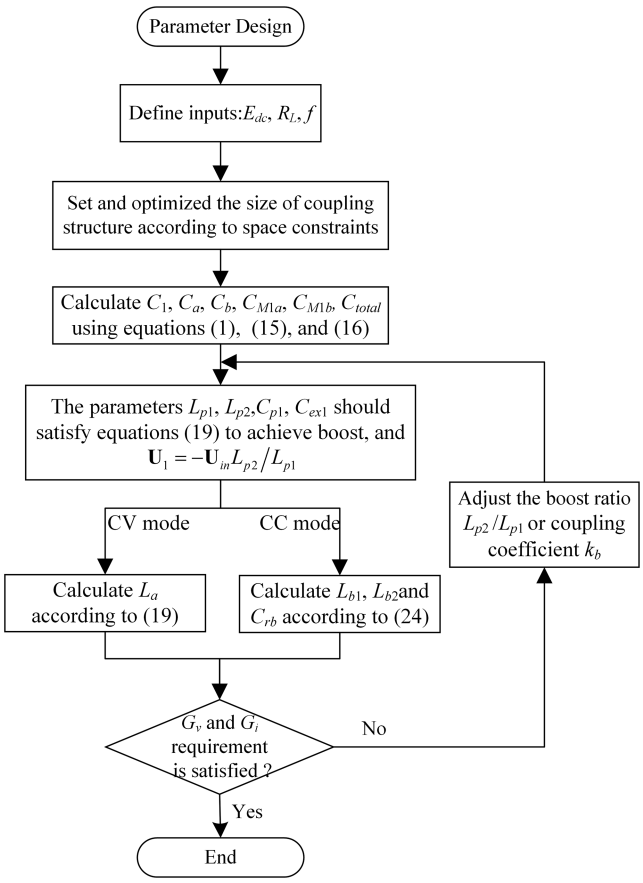

Fig. 15. Parameters design method.

flowchart, and the flowchart illustrates the relationship between all resonant network elements. Generally, the value of operating frequency f is set according to the mutual capacitance combined with the requirement of the inductor [10], [26]. The transmission distance is specified according to the restrictions of application fields. The input voltage $E_{\rm dc}$ and the resistance load R_L are determined by the requirement of the application.

TABLE III
SYSTEM PARAMETERS

Symbol	Parameter	Value
E_{dc}	Input voltage	120 V
L_{p1}	Primary side resonant inductor	2.55 uH
R_{p1}	Parasitic resistance of L_{p1}	0.23 Ω
C_{p1}	Primary side resonant capacitor	2.816 nF
L_{p2}	Primary side resonant inductor	25.4 uH
R_{p2}	Parasitic resistance of L_{p2}	0.85 Ω
C_{ex1}	Primary side extra capacitor	238.4 pF
L_a	Secondary side resonant inductor	27.06 uH
R_a	Parasitic resistance of L_a	0.93 Ω
L_{b1}	Secondary side resonant inductor	11.96 uH
R_{b1}	Parasitic resistance of L_{b1}	0.62 Ω
L_{b2}	Secondary side resonant inductor	6 uH
R_{b2}	Parasitic resistance of L_{b2}	0.31 Ω
C_{rb}	Secondary side resonant capacitor	1.09 nF
R_{La}	Resistor of load a	5–20 Ω
R_{Lb}	Resistor of load b	500–1500 Ω
k_{ab}	Coupling coefficient between C_a and C_b	0.4
M_{ab}	Mutual inductance between L_a and L_b	2.725 uH
f	Resonant frequency	1.97 MHz

The coupler could be obtained according to the application requirement, and the coupler could be further optimized according to the analysis in Section IV-A. Once the size of the coupler is determined, the capacitances C_1, C_a, C_b, and mutual capacitances $C_{M1\,a}$, $C_{M1\,b}$ can be calculated using (1) and (15). The parameter $C_{\rm total}$ can be calculated using (16), and the primary side compensation should satisfy (19). When the system works in CV mode, the secondary side compensation only needs an inductor L_a, and the parameter L_a can be calculated using (19). Similarly, when the system works in CC mode, the M topology is selected as a secondary side compensation network, and the parameters L_{b1}, L_{b2} and C_{rb} can be obtained using (24).

V. SIMULATION AND EXPERIMENT

A. Simulation Results

LT-spice is used to simulate the performance of the proposed double-receiver SCC-WPT system. The circuit in Fig. 7 is used to model the designed prototype system. The input voltage $E_{\rm dc}$ is set to 120 V, and the frequency is selected as 1.97 MHz to consistent with the experiment. According to the parameter design flowchart in Fig. 15, system parameters are given in Table III. The parasitic resistance of the inductor is tested by using the LCR meter (GWINSTEK LCR-8230).

When the R_{La} is 10Ω and R_{Lb} is 750Ω, the simulated results of the output voltage $\mathbf{U}_{\rm in}$, current $\mathbf{I}_{\rm in}$, dc input current $I_{\rm out\,a}$, and dc output voltage $U_{\rm out\,b}$ are illustrated in Fig. 16. The simulation results show that the G_{va} and G_{ib} are 0.19 and 0.0022.

B. Experiment Setup

A double-receiver compact SCC-WPT prototype is built based on the theoretical analysis and simulation research in the

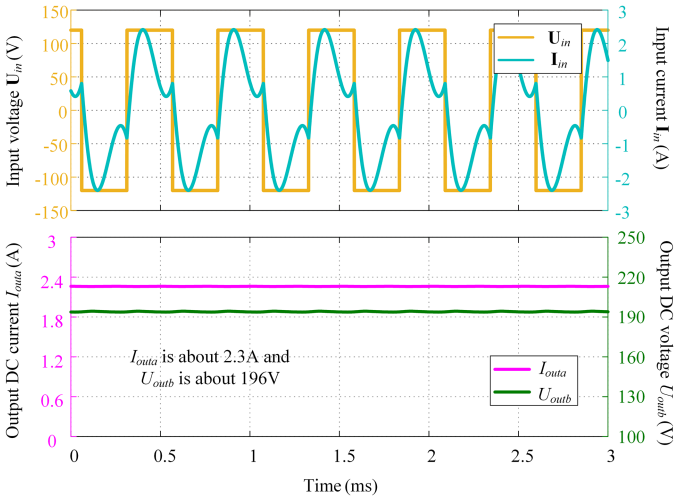

Fig. 16. Simulated waveform of the input and output.

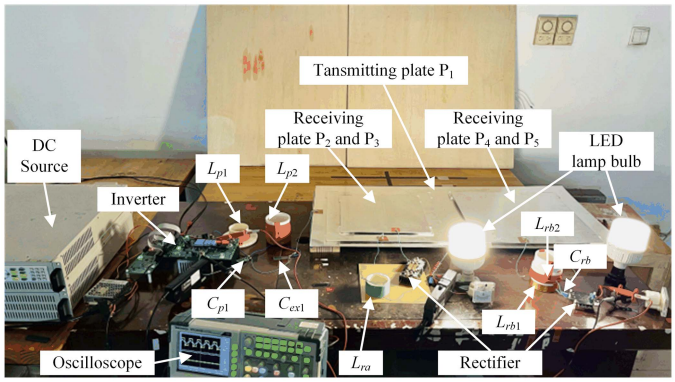

Fig. 17. Experimental prototype of the proposed double-receiver compact SCC-WPT.

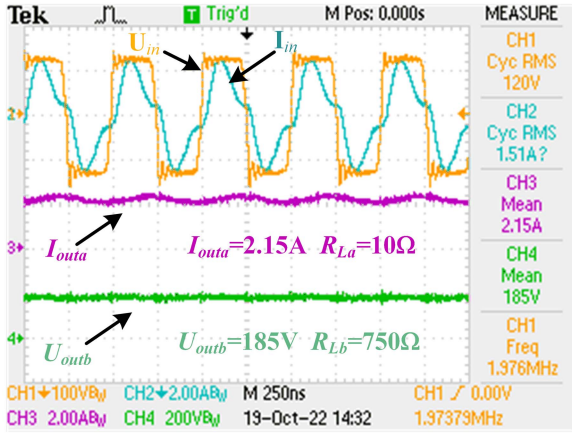

Fig. 18. Experimental waveforms of the inverter and the output of two receivers when R_{La}=10 Ω and R_{Lb}=750 Ω.

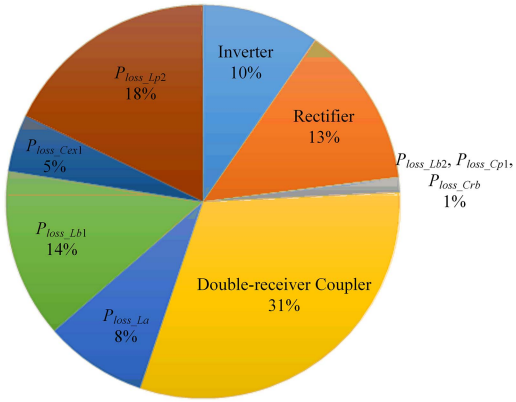

Fig. 19. Power loss distribution of the proposed system components.

following sections. Fig. 17 shows the experimental prototype, where the coupler adopted the aluminum plate, and the size of each metal plate is given in Table I. The actual measured capacitance parameters are consistent with the simulation parameters, as given in Table II. Table III gives the detailed experiment prototype parameters. In the experiment, the driver chip of MOSFETs is adopted DSP TMS320, and the dominant frequency is 150 MHz. So that the accurate frequency of 2 MHz could not be obtained, and the 1.97 MHz is selected as a resonance frequency in this article. It should be noted that the capacitances C_{12}, C_{23}, C_{14}, and C_{45} are slightly greater than the simulation values due to the small square with acrylic used to separate the plate. The actual measurement values of capacitance C_{12}, C_{23}, C_{14}, and C_{45} are, respectively, 330, 231, 312, and 520 pF by testing with the LCR meter.

The distance between the transmitter and receiver plates is 5 mm, the coupling capacitance C_{M1a} is about 5.92 pF, and the C_{M1b} is about 7.27pF. Current probes (CYBERTEK CP8150A) and voltage differential probes (DP6150) are adopted to acquire experimental data. As designing the resonant parameters in the experiment, tuning the system to the inductance region to reducing switching loss. Considering the influence of the higher operating frequency of the system (1.97 MHz) on the loss of the rectifier and inverter. The full-bridge inverter and rectifier are adopted silicon carbide (SiC) MOSFETs IMZ120R045M1 and SiC diodes GHXS030A120S to reduce the junction capacitance of the device. The inductors L_{p1}, L_{p2}, L_{ra}, L_{rb1}, and L_{rb2} have an air core and are made with 0.04 diameter 600-strand Litz-wire, thereby reducing the magnetic loss, the sectional area and peak withstand current is mainly considered in the inductor selection. The inductors L_{rb1} and L_{rb2} are wind on two PVC tubes, and the outer diameter of the two PVC tubes is 75 and 85 mm, respectively. Thus, the inductor L_{b1} has a total of 11 turns, and inductance L_{b2} has 6 turns. High-frequency C0G chip capacitors and film capacitance are used as resonant capacitors. The inductors L_{rb1} and L_{rb2} are wind on two PVC tubes, and the outer diameter of the two PVC tubes is 75 and 85 mm, respectively. Thus the inductor L_{b1} has a total of 11 turns, and inductance L_{b2} has 6 turns. High-frequency C0G chip capacitors and film capacitance are used as resonant capacitors.

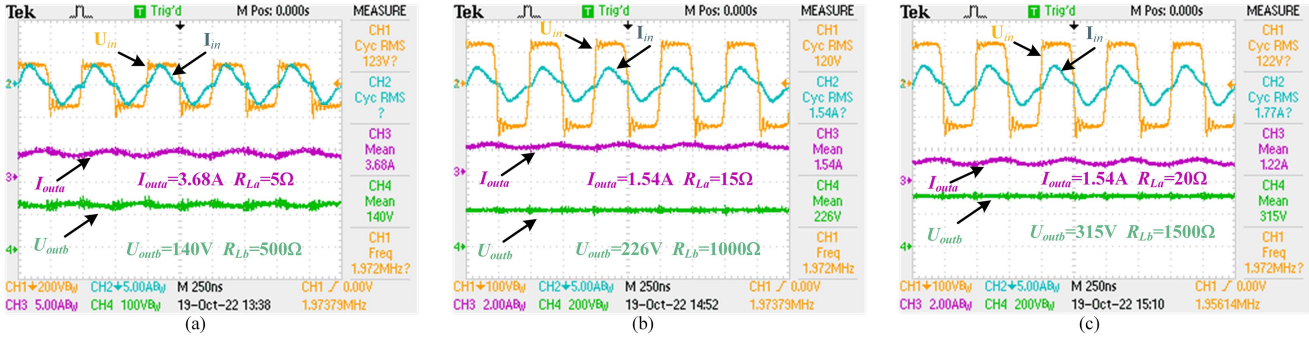

Fig. 20. Proposed system with the different load resistance. (a) R_{La}=5 Ω and R_{Lb}=500 Ω.(b) R_{La}=15 Ω and R_{Lb}=1000 Ω. (c) R_{La}=20 Ω and R_{Lb}=1500 Ω.

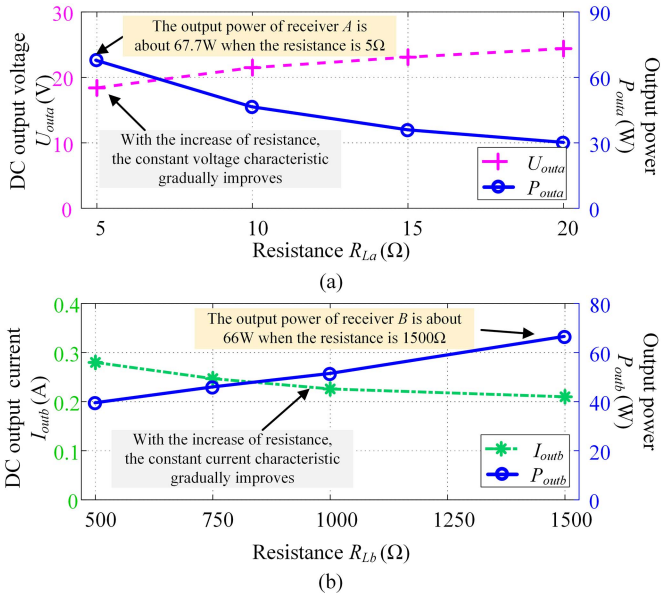

Fig. 21. Output characteristic of the proposed system. (a) Receiver A. (b) Receiver B.

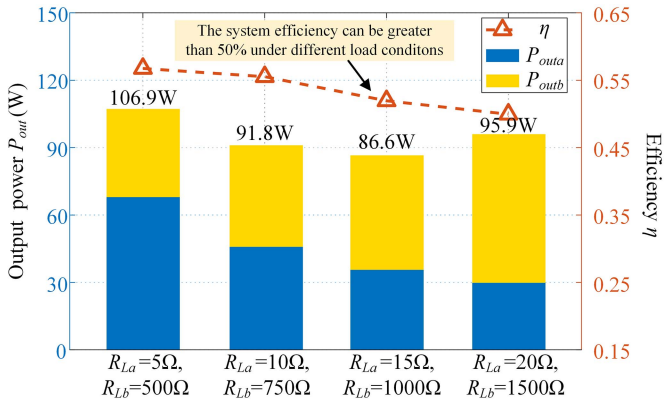

Fig. 22. Measured values of each dc–dc efficiency and the output power P_{out} at different load resistance situations.

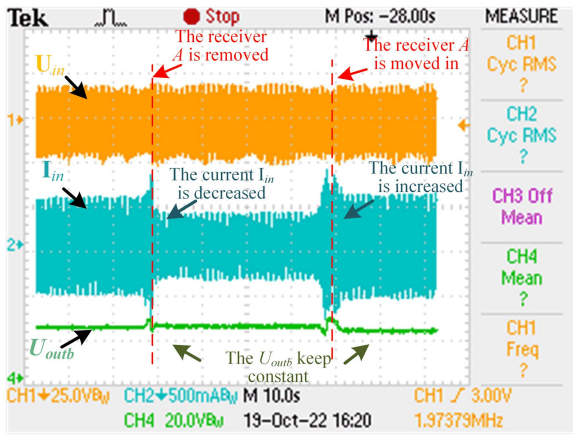

Fig. 23. Waveforms of the dynamic process.

C. CV and CC Performance Against Load Variation

Fig. 17 shows that both bulbs have been lighted at the same time. The LED lamp bulb is used for photography and display, and different values of resistances are adopted as the load in the subsequent measurement. Fig. 18 shows the experimental waveforms of the inverter and the output of two receivers when $R_a = 10\Omega$ and $R_b = 750\,\Omega$. The experiment results are basically consistent with the simulation results in Fig. 16. The current-probe and Voltage-probe will influence the SCC-WPT system, but this system is almost unaffected when the current-probe test in the load resistance R_L [23]. The pointer ammeter is also used to verify the accuracy of the current probe. In addition, receiver B adopts the M topology. The resistance R_{Lb} is isolated from the coupler, and the voltage-probe cannot influence the system. The voltage probe is used to test the receiver B because the current gain is too small, and the voltage measurement will be more accurate.

The experimental waveforms show that receiver A achieved about 46.2 W output power and receiver B achieved about 45.6W output power. At this time, the input voltage E_{dc} and input current I_{dc} are 120 V and 1.36 A, and the dc–dc efficiency of the proposed system is 56.2%. According to the experimental results from Fig. 18, the voltage gains of receiver A and the

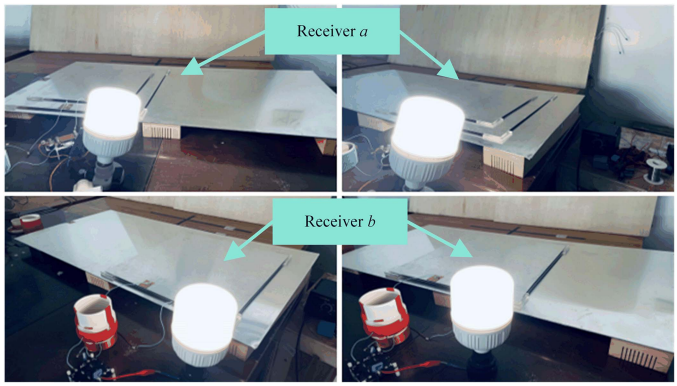

Fig. 24. Experimental free-positioning feature.

current gain of receiver *B* are about 0.18 and 0.0021, respectively. The experimental results are accordant to simulated results. According to the measured capacitance, combining the formula (22) and (27), the voltage gains G_{va} and current gains G_{ib} are about 0.24 and 0.0026, respectively. The error of the output gain among experimental, simulation, and theoretical mainly come from the system loss, and there is an element of parameter error that leads to output gain errors.

For the proposed system, the system losses mainly include converter loss, coupler loss, inductor loss ($P_{\text{loss\_}Lp1}$, $P_{\text{loss\_}Lp2}$, $P_{\text{loss\_}La}$, $P_{\text{loss\_}Lb1}$, and $P_{\text{loss\_}Lb2}$), and capacitor loss ($P_{\text{loss\_}Cp1}$, $P_{\text{loss\_}Cex1}$, and $P_{\text{loss\_}Crb}$). The power losses of a converter consist of conduction losses and switching losses of diodes and switching devices, such as MOSFETs and IGBTs. The calculations of converter loss are mainly based on [33]. The inductor loss could be calculated from each current and parasitic resistance of the inductor and the capacitor parasitic resistance could be calculated according to [34]. The remaining losses are assumed to be in the coupler and the losses of earth resistance. The loss distribution of the proposed system when $R_{La} = 10\ \Omega$ and $R_{Lb} = 750\ \Omega$ is depicted in Fig. 19. The inductor loss and coupler loss dissipate approximately 64% of the power loss. Most of the power loss comes from the converter and parasitic resistance of the inductors due to the high switching frequency. In addition, the lower part of the source is directly connected to the earth's ground in the power socket on the wall with a wire in the experiment. In our lab, the floor is made of concrete containing iron bars, the conductivity of the floor is not comparable with soil, thus earth resistance is high and resulting in some losses. At the same time, the constant mode is related to the system's efficiency. The efficiency will be further optimized by using high-quality electronic elements in the future. Future research will focus on system optimization to minimize losses and increase efficiency.

Fig. 20 shows the experimental results with different load resistances. According to Fig. 20, the output current of receiver *A* and the output voltage of receiver *B* is shown in Fig. 21. The change rate of the output voltage $U_{\text{out}\,a}$ in receiver *A* is about 24.6% when the resistance R_{La} is changed from 5 to 20 Ω, and the change rate of the output current $I_{\text{out}\,b}$ in receiver *B* is about 25% when the resistance R_{Lb} is changed from 500 to 1500 Ω. To better display the effect and characteristic of the system, the load resistance R_{Lb} is chosen to be 500–1500 Ω to achieve a larger output power in the experiments, which results in a larger output voltage. From Fig. 21, the change rate of voltage in receiver *A* and current in receiver *B* are also decreased gradually when the load resistance is increased. Therefore, receiver *A* and receiver *B* could achieve a better constant effect at the conditions of light load and heavy load, respectively. The inductor with a high-quality factor will be adopted and analysis the loss model of the coupler in the future research, which can be used to reduce the system loss and improve its constant range.

According to the experimental results under different load resistance, Fig. 22 shows the dc–dc efficiency and output power of two receivers under different load situations. The total output power is 106.9, 91.8, 86.6, and 95.9 W respectively. The input dc current is measured to be 1.57, 1.36, 1.39, and 1.6 A. Therefore, the efficiency of the system is 56.8%, 56.2%, 52%%, and 50% when supplied power to the two receivers with different load resistance.

D. Experiment With Load-Independent and Free-Positioning Feature

In the experimental of the independence between receivers, the dc voltage E_{dc} is set to 25 V for safety. Fig. 23 shows the dynamic process when receiver *A* is removed and then moved in. The output voltage of receiver *B* could be kept constant basically when the receiver is moved in or removed, and the system can realize the independence between the two receivers. It should be explained that the physical movement of the receiver is carried out manually, and the overcurrent of $\mathbf{I}_{\text{in}}$ is caused by the coupling change during the receiver moving process. Thus, the experimental results of each operation are slightly different due to the inconsistence in the manual movement. When receiver *A* is removed, the $U_{\text{out}\,b}$ is changed from 22.5 to 23.2 V, and the change rate is about 3.1%. When receiver *A* is moved in, the $U_{\text{out}\,b}$ is changed from 23.2 to 21.9 V, and the change rate is about 5.6%.

The transmitting plate P_1 of the proposed system is only an aluminum plate. The coupler has the equivalent mutual capacitances at any position above the P_1. Thus, the receiver is able to receive stable power within the range of P_1. Fig. 24 shows the lighting at the different points of the LED lamp bulb when the input voltage is set to 40V. Both bulbs *A* and *B* could maintain the same lighting when the receiving plate is placed on a different point. To better shows the output change trend when the receiver at different position of plate P_1, the experiment waveforms of the output of receivers when the receivers at different positions or with rotational offset are added, as shown in Fig. 25. When receiver *A* placed at different positions within the range of the transmitting plate, the output of receiver *A* could be almost kept constant and the change rate is about 5.7%. In the same case, the change rate of receiver *B* is about 1.6%. In the rotational offset case, the output of the system can also remain stable.

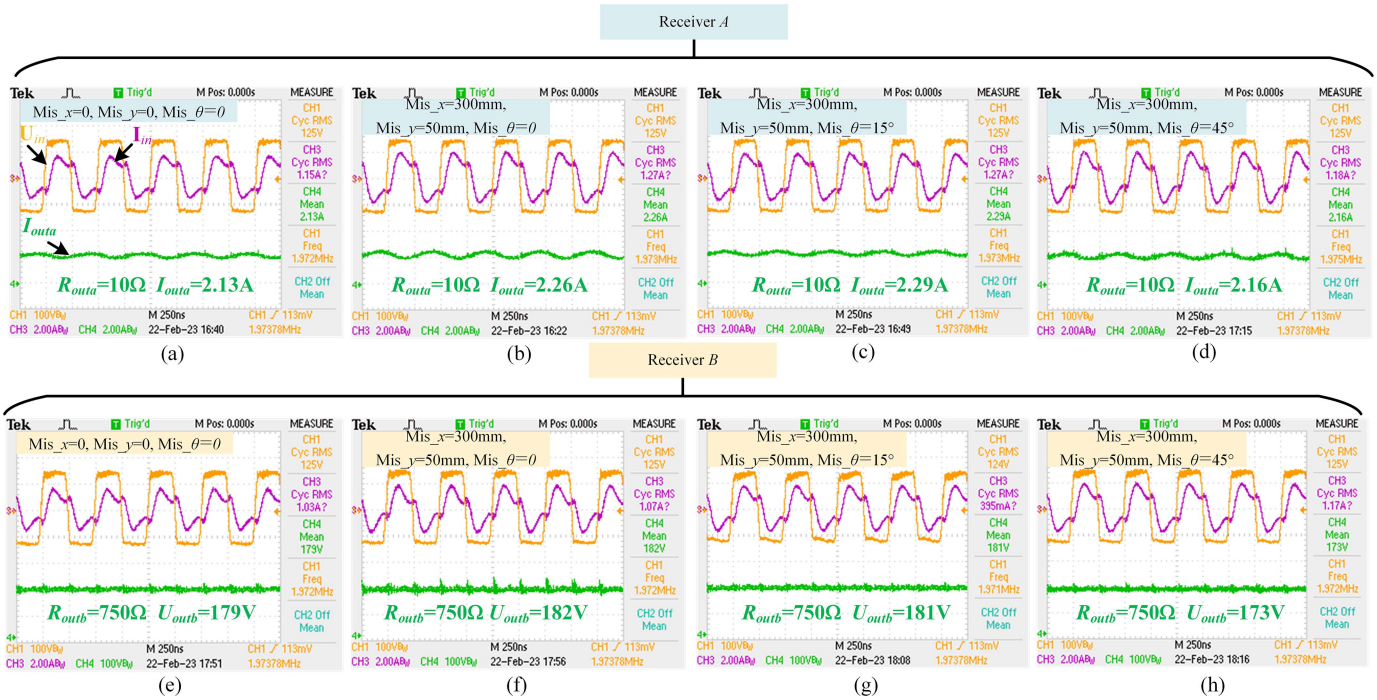

Fig. 25. Experimental waveform with free-positioning feature. Only receiver A: (a) Mis_$x = 0$, Mis_$y = 0$, Mis_$\theta = 0$. (b) Mis_$x = 300$ mm, Mis_$y = 50$ mm, Mis_$\theta = 0$. (c) Mis_$x = 300$ mm, Mis_$y = 50$ mm, Mis_$\theta = 15°$.(d) Mis_$x = 300$ mm, Mis_$y = 50$ mm, Mis_$\theta = 45°$. Only reveiver B: (e) Mis_$x = 0$, Mis_$y = 0$, Mis_$\theta = 0$. (f) Mis_$x = 300$ mm, Mis_$y = 50$ mm, Mis_$\theta = 0$. (g) Mis_$x = 300$ mm, Mis_$y = 50$ mm, Mis_$\theta = 15°$. (h) Mis_$x = 300$ mm, Mis_$y = 50$ mm, Mis_$\theta = 45°$.

TABLE IV
COMPARISONS WITH OTHER WORKS

Proposed in	[15]	[16]	[21]	This article
Adopted technology	CPT	CPT	CPT	SCC-WPT
Free-positioning Feature	x- and y-direction	x- and y-direction	y-direction	x-, y-, and θ-direction
No controls	Yes	No	Yes	Yes
Multiple receiver	No	No	Yes	Yes
Load-independent	N/A	N/A	Yes	Yes
Output power	5–15 W	5 W	Total 14.1 W	Total 106.9 W
Mutual capacitance C_M	Not mentioned	Not mentioned	270 pF	5.9–7.3 pF
Efficiency	50%–66%	81.2%–86.8%	67%–83.6%	56.2%
Frequency	1–3.45 MHz	2.28 MHz	10 MHz	1.97 MHz
Constant-output	CC	Not mentioned	CV	CC and CV

The coupler is over the range of the transmitting plate a little when the rotation angle is 45°; even so, the change rate is just 4.4% and 4.9% in receiver A and receiver B. Meanwhile, the output current $I_{\mathrm{out}\,a}$ and output voltage $U_{\mathrm{out}\,b}$ almost remain unchanged compared with the full receiver state, as shown in Fig. 18.

E. Comparison With Other Works

Table IV gives the performance indexes of existing systems and this article. In [15], the proposed novel capacitive coupler array has a free-positioning feature, the system has a good performance, and is suitable for mobile devices charging. Yuan et al. [16] proposed an antioffset interdigital electrode capacitive coupler for mobile desktop charging with a switching control method, which can be kept 5 W output power with over 80% efficiency when the device is moved in the x-direction or y-direction. However, these systems only keep stable power when the misalignment happens in the x-direction or y-direction. When the rotational offset happens, these systems cannot achieve constant output. Lillholm et al. [21] proposed a multiple-output CPT system with the load-independent characteristic. But, the receiver only moves freely in one direction. This article proposed a double-receiver SCC-WPT system with load-independent, in which one receiver can achieve CV output while another receiver can achieve CC output. Compared with existing systems, the proposed system has a better free-positioning feature, and the system could transfer power to two devices.

TABLE V
Y-PARAMETERS OF THE COUPLER

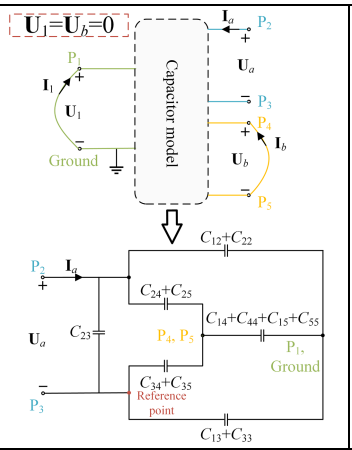	$\begin{cases} A_2 = C_{24}+C_{25} \\ B_2 = C_{12}+C_{22} \\ D_2 = C_{34}+C_{35} \\ E_2 = C_{13}+C_{33} \\ F_2 = C_{14}+C_{44}+C_{15}+C_{55} \end{cases}$	$\begin{cases} C_{Xa} = (A_2+B_2+D_2+E_2)F_2+(A_2+D_2)(B_2+E_2) \\ C_a = C_{23}+\dfrac{1}{C_{Xa}}\begin{pmatrix} A_2((B_2+F_2)(D_2+E_2)+D_2E_2) \\ +B_2(D_2F_2+D_2E_2+E_2F_2) \end{pmatrix} \\ C_{Mba} = \dfrac{1}{C_{Xa}}\begin{pmatrix} (C_{24}C_{35}-C_{25}C_{34})(B_2+E_2+F_2) \\ +(C_{14}+C_{44})(B_2C_{35}-E_2C_{25}) \\ +(C_{15}+C_{55})(E_2C_{24}-B_2C_{34}) \end{pmatrix} \\ C_{M1a} = \dfrac{1}{C_{Xa}}\begin{pmatrix} C_{33}(A_2B_2+A_2F_2+B_2D_2+B_2F_2) \\ -C_{22}(A_2E_2+D_2E_2+D_2F_2+E_2F_2) \\ -(C_{44}+C_{55})(A_2E_2-B_2D_2) \end{pmatrix} \end{cases}$	$\begin{cases} Y_{12} = -j\omega C_{M1a} \\ Y_{22} = j\omega C_a \\ Y_{32} = -j\omega C_{Mba} \end{cases}$
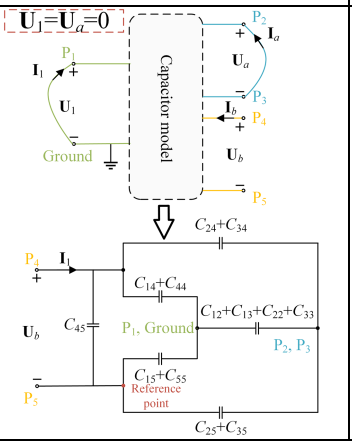	$\begin{cases} A_3 = C_{14}+C_{44} \\ B_3 = C_{24}+C_{34} \\ D_3 = C_{15}+C_{55} \\ E_3 = C_{25}+C_{35} \\ F_3 = C_{12}+C_{13}+C_{22}+C_{33} \end{cases}$	$\begin{cases} C_{Xb} = (A_3+B_3+D_3+E_3)F_3+(A_3+D_3)(B_3+E_3) \\ C_b = C_{45}+\dfrac{1}{C_{Xb}}\begin{pmatrix} A_3((B_3+F_3)(D_3+E_3)+D_3E_3) \\ +B_3(D_3F_3+D_3E_3+E_3F_3) \end{pmatrix} \\ C_{M1b} = \dfrac{1}{C_{Xb}}\begin{pmatrix} (C_{14}C_{55}-C_{15}C_{44})(B_3+E_3+F_3) \\ +(C_{12}+C_{13})(B_3C_{55}-E_3C_{44}) \\ +(C_{22}+C_{33})(E_3C_{14}-B_3C_{15}) \end{pmatrix} \\ C_{Mab} = \dfrac{1}{C_{Xb}}\begin{pmatrix} C_{35}(A_3B_3+A_3F_3+B_3D_3+B_3F_3) \\ -C_{34}(A_3E_3+D_3E_3+D_3F_3+E_3F_3) \\ -(C_{13}+C_{33})(A_3E_3-B_3D_3) \end{pmatrix} \end{cases}$	$\begin{cases} Y_{13} = -j\omega C_{M1b} \\ Y_{23} = -j\omega C_{Mab} \\ Y_{33} = j\omega C_b \end{cases}$

VI. CONCLUSION

In this article, a double-receiver SCC-WPT system with constant output is proposed for mobile device charging/supply, which the output of receivers is independent of each other. A three-plate compact coupler is proposed to increase coupling capacitance and improve the system's performance. The full capacitance model of the coupler with two receivers is analyzed and simplified, and the equivalent controlled source model of the coupler is established. Based on the demand of mobile devices for constant output, the *LCLC*-S and *LCLC*-M topology is proposed to achieve CV output and CC output, respectively. The resonance conditions of the system are analyzed, and the output gain of the system is derived. Then the coupler is studied to obtain a high output gain. Finally, a double-receiver SCC-WPT prototype is built based on the proposed topology and method, and the experiment has verified the correctness of the theoretical analysis.

The advantages of the proposed CPT system are listed as follows.

1) When the load resistance variation, one receiver can achieve CV output while the other can achieve CC output in the proposed double-receiver SCC-WPT system.
2) The output characteristic of the receiver could maintain almost unchanged when another receiver is moved in or removed.
3) The proposed system could provide free-positioning feature (*x*-, *y*-, and θ-direction) charging/supply within the range of the transmitting plate.

It should be noted that converter design and parameter optimization is the subject that is worth studying when applied to the actual product. It can improve the efficiency and CV/CC characteristics of the system. Meanwhile, the problem of safety and physical environmental effect also cannot be ignored, which will lead to whether the product is practical. Future research will focus on these subjects and improve the performance and security of the system.

APPENDIX

The admittance parameters Y_{12}, Y_{22}, and Y_{32} can be obtained when the voltage $\mathbf{U}_1$ and $\mathbf{U}_b$ are set to zero. Meanwhile, the parameters Y_{13}, Y_{23}, and Y_{33} are acquired with $\mathbf{U}_1$ and $\mathbf{U}_a$ are zero. These *Y*-parameters could be calculated through the same light of analysis in Section II, as given in Table V.

ACKNOWLEDGMENT

The authors of this article gratefully acknowledge the support of the China National Center for International Research on Wireless Power Transfer Technology.

REFERENCES

[1] Y. Wang, H. Zhang, and F. Lu, "Review, analysis, and design of four basic CPT topologies and the application of high-order compensation networks," *IEEE Trans. Power Electron.*, vol. 37, no. 5, pp. 6181–6193, May 2022.

[2] C. Cai, X. Liu, S. Wu, X. Chen, W. Chai, and S. Yang, "A misalignment tolerance and lightweight wireless charging system via reconfigurable capacitive coupling for unmanned aerial vehicle applications," *IEEE Trans. Power Electron.*, vol. 38, no. 1, pp. 22–26, Jan. 2023.

[3] S. Hagen, M. Tisler, J. Dai, I. P. Brown, and D. C. Ludois, "Use of the rotating rectifier board as a capacitive power coupler for brushless wound field synchronous machines," *IEEE J. Emerg. Sel. Topics Power Electron.*, vol. 10, no. 1, pp. 170–183, Feb. 2022.

[4] B. Luo, A. P. Hu, H. Munir, Q. Zhu, R. Mai, and Z. He, "Compensation network design of CPT systems for achieving maximum power transfer under coupling voltage constraints," *IEEE J. Emerg. Sel. Topics Power Electron.*, vol. 10, no. 1, pp. 138–148, Feb. 2022.

[5] B. Regensburger, S. Sinha, A. Kumar, S. Maji, and K. K. Afridi, "High-performance multi-MHz capacitive wireless power transfer system for EV charging utilizing interleaved-foil coupled inductors," *IEEE J. Emerg. Sel. Topics Power Electron.*, vol. 10, no. 1, pp. 35–51, Feb. 2022.

[6] J. Xia, X. Yuan, S. Lu, J. Li, S. Luo, and S. Li, "A two-stage parameter optimization method for capacitive power transfer systems," *IEEE Trans. Power Electron.*, vol. 37, no. 1, pp. 1102–1117, Jan. 2022.

[7] S. Zang, Q. Zhu, L. Zhao, and A. P. Hu, "Capacitive power transfer system with integrated wide bandwidth communication," *IEEE Trans. Power Electron.*, vol. 37, no. 8, pp. 8805–8810, Aug. 2022.

[8] X. Dai, M. Sun, P. Deng, R. Wang, and Y. Su, "Asymmetric bidirectional capacitive power transfer method with push–pull full-bridge hybrid topology," *IEEE Trans. Power Electron.*, vol. 37, no. 11, pp. 13902–13913, Nov. 2022.

[9] T. Chen, C. Cheng, H. Cheng, C. Wang, and C. C. Mi, "A multi-load capacitive power relay system with load-independent constant current outputs," *IEEE Trans. Power Electron.*, vol. 37, no. 5, pp. 6144–6155, May 2022.

[10] Z. Liu, Y.-G. Su, Y.-M. Zhao, A. P. Hu, and X. Dai, "Capacitive power transfer system with double T-type resonant network for mobile devices charging/supply," *IEEE Trans. Power Electron.*, vol. 37, no. 2, pp. 2394–2403, Feb. 2022.

[11] X. Qing, Y. Su, A. P. Hu, X. Dai, and Z. Liu, "Dual-loop control method for CPT system under coupling misalignments and load variations," *IEEE J. Emerg. Sel. Topics Power Electron.*, vol. 10, no. 4, pp. 4902–4912, Aug. 2022.

[12] B. Minnaert, F. Mastri, A. Costanzo, M. Mongiardo, and N. Stevens, "Optimizing the power output for a capacitive wireless power transfer system with *N* receivers," in *Proc. IEEE Wireless Power Transfer Conf.*, 2019, pp. 351–354.

[13] R. He, P. Zhao, G. Ning, K. Yue, Y. Liu, and M. Fu, "Optimal driving and loading scheme for multiple-receiver inductive power transfer," *IEEE Trans. Ind. Electron.*, vol. 69, no. 12, pp. 12665–12675, Dec. 2022.

[14] J. Lu, G. Zhu, D. Lin, Y. Zhang, H. Wang, and C. C. Mi, "Realizing constant current and constant voltage outputs and input zero phase angle of wireless power transfer systems with minimum component counts," *IEEE Trans. Intell. Transp. Syst.*, vol. 22, no. 1, pp. 600–610, Jan. 2021.

[15] J.-Q. Zhu et al., "A novel capacitive coupler array with free-positioning feature for mobile tablet Applications," *IEEE Trans. Power Electron.*, vol. 34, no. 7, pp. 6014–6019, Jul. 2019.

[16] H. Yuan et al., "A novel anti-offset interdigital electrode capacitive coupler for mobile desktop charging," *IEEE Trans. Power Electron.*, vol. 38, no. 3, pp. 4140–4151, Mar. 2023.

[17] T. Feng, Z. Zuo, Y. Sun, X. Dai, X. Wu, and L. Zhu, "A reticulated planar transmitter using a three-dimensional rotating magnetic field for free-positioning omnidirectional wireless power transfer," *IEEE Trans. Power Electron.*, vol. 37, no. 8, pp. 9999–10015, Aug. 2022.

[18] B. H. Choi, E. S. Lee, Y. H. Sohn, G. C. Jang, and C. T. Rim, "Six degrees of freedom mobile inductive power transfer by crossed dipole Tx and Rx coils," *IEEE Trans. Power Electron.*, vol. 31, no. 4, pp. 3252–3272, Apr. 2016.

[19] Y.-G. Su, S.-Y. Xie, A. P. Hu, C.-S. Tang, W. Zhou, and L. Huang, "Capacitive power transfer system with a mixed-resonant topology for constant-current multiple-pickup applications," *IEEE Trans. Power Electron.*, vol. 32, no. 11, pp. 8778–8786, Nov. 2017.

[20] W. Zhou, Q. Gao, L. He, B. Luo, R. Mai, and Z. He, "Design of CPT system with multiple constant output voltage pickups using inverse hybrid parameters of capacitive coupler," *IEEE Trans. Ind. Appl.*, vol. 58, no. 1, pp. 1061–1070, Jan./Feb. 2022.

[21] M. B. Lillholm, Y. Dou, X. Chen, and Z. Zhang, "Analysis and design of 10-MHz capacitive power transfer with multiple independent outputs for low-power portable devices," *IEEE J. Emerg. Sel. Topics Power Electron.*, vol. 10, no. 1, pp. 149–159, Feb. 2022.

[22] L. J. Zou, Q. Zhu, C. W. Van Neste, and A. P. Hu, "Modeling single wire capacitive power transfer system with strong coupling to ground," *IEEE J. Emerg. Sel. Topics Power Electron.*, vol. 9, no. 2, pp. 2295–2302, Apr. 2021.

[23] Z. Liu, Y. Su, H. Hu, Z. Deng, and R. Deng, "Research on transfer mechanism and power improvement technology of the SCC-WPT system," *IEEE Trans. Power Electron.*, vol. 38, no. 1, pp. 1324–1335, Jan. 2023.

[24] X. Gao et al., "Capacitive power transfer through virtual self-capacitance route," *Inst. Eng. Technol. Power Electron*, vol. 11, no. 6, pp. 1110–1118, 2018.

[25] F. Lu, H. Zhang, and C. Mi, "A two-plate capacitive wireless power transfer system for electric vehicle charging applications," *IEEE Trans. Power Electron.*, vol. 33, no. 2, pp. 964–969, Feb. 2018.

[26] S. Li, Z. Liu, H. Zhao, L. Zhu, C. Shuai, and Z. Chen, "Wireless power transfer by electric field resonance and its application in dynamic charging," *IEEE Trans. Ind. Electron.*, vol. 63, no. 10, pp. 6602–6612, Oct. 2016.

[27] X. Gao et al., "Design and analysis of a new hybrid wireless power transfer system with a space-saving coupler structure," *IEEE Trans. Power Electron.*, vol. 36, no. 5, pp. 5069–5081, May 2021.

[28] Y. Cui, "A simple and convenient calculation of the capacitance for an isolated conductor plate," *Eur. J. Phys.*, vol. 17, no. 6, pp. 363–364, 1996.

[29] T. M. Minteer, "The many capacitance terms of two parallel disks in free space," *Eur. J. Phys.*, vol. 35, no. 3, pp. 99–106, 2014.

[30] H. Nishiyama and M. Nakamura, "Form and capacitance of parallel plate capacitors," *IEEE Trans. Compon. Packag. Munuf. Tech.–Part A*, vol. 17, no. 3, pp. 477–484, Sep. 1994.

[31] W. Zhang and C. C. Mi, "Compensation topologies of high-power wireless power transfer systems," *IEEE Trans. Veh. Technol.*, vol. 65, no. 6, pp. 4768–4778, Jun. 2016.

[32] Y. Fang, B. M. H. Pong, and R. S. Y. Hui, "An enhanced multiple harmonics analysis method for wireless power transfer Systems," *IEEE Trans. Power Electron.*, vol. 35, no. 2, pp. 1205–1216, Feb. 2020.

[33] B. X. Nguyen et al., "An efficiency optimization scheme for bidirectional inductive power transfer systems," *IEEE Trans. Power Electron.*, vol. 30, no. 11, pp. 6310–6319, Nov. 2015.

[34] F. Lu, H. Zhang, H. Hofmann, and C. Mi, "A high efficiency 3.3 kW loosely-coupled wireless power transfer system without magnetic material," in *Proc. IEEE Energy Convers. Congr. Expo.*, 2015, pp. 2282–2286.

Zhe Liu received the B.E. degree in electrical engineering from the Chongqing University of Technology, Chongqing, China, in 2014, and the M.E. degree from the College of Electrical Engineering, Kunming University of Science and Technology, Kunming, China, in 2017. He is currently working toward the Ph.D. degree in control theory and control engineering with the School of Automation, Chongqing University, Chongqing, China.

His research interests include capacitive power transfer and the single capacitive coupled wireless power transfer.

Hongsheng Hu (Member, IEEE) received the B.Eng. degree in electrical engineering and automation and the Ph.D. degree in power electronics and power drives from Huazhong University of Science and Technology, Wuhan, China, in 2014 and 2021, respectively.

He is currently a Postdoctoral Research Scholar with the School of Automation, Chongqing University. His research interests include modularized IPT systems, bidirectional IPT systems, capacitive power transfer, and power electronics.

Yu-Gang Su (Member, IEEE) received the B.E. and M.E. degrees in industry automation and the Ph.D. degree in control theory and control engineering from Chongqing University, Chongqing, China, in 1985, 1993 and 2004, respectively.

From 2008 to 2009, he was a Visiting Scholar with the University of Queensland, Brisbane, Australia. He is currently a Professor with the School of Automation, Chongqing University. His research interests include power electronics, control theory and applications, wireless power transfer.

Yue Sun (Member, IEEE) received the B.E. degree in electrical engineering, the M.E. degree in industry automation and the Ph.D. degree in mechanical electrical integrated manufacturing from Chongqing University, Chongqing, China, in 1982, 1988, and 1995, respectively.

In 1997, he was a Senior Visiting Scholar with the University of Valenciennes, Valenciennes, France. He is currently a Professor with the School of Automation, Chongqing University. His current research interests include automatic control, wireless power transfer, and power electronics applications.

Fengwei Chen was born in Chongqing, China. He received the B.Eng. degree in automation and the M.Eng. degree in control theory and control engineering from Wuhan University, Wuhan, China, in 2009 and 2011, respectively, and the Ph.D. degree in automatic control from the Université de Lorraine, Nancy, France, in 2014.

From 2015 to 2016, he was a Lecturer with the Dalian University of Technology, Dalian, China. From 2017 to 2020, he was an Associate Researcher with Wuhan University, Wuhan, China. Since 2021, he has been with Chongqing University, Chongqing, China, where he is currently an Associate Professor. His research interests include system identification and parameter estimation, with applications to wireless power transfer.

Pengqi Deng received the B.E. degree in automation in 2015 from College of Automation, Chongqing University, Chongqing, China, where he is currently working toward the Ph.D. degree in the control theory and control engineering.

His research interests include modeling and control optimization of the wireless power transfer.